Fast Ion Confinement Analysis for NCSX

I. Introduction

Neutral beams will provide one of the primary heating methods for NCSX; up to 6 Mw of beam power will be available in the 40 to 50 keV energy range. These beams will be injected tangentially in both the co- and counter- directions. In addition to plasma heating, beams are also expected to provide a means for external control over the level of toroidal plasma rotation velocity and its profile.

NCSX has been designed to be as nearly toroidally symmetric as possible in magnetic Boozer coordinates[1]. This leads to improved energetic beam ion confinement and higher predicted heating efficiencies in comparison to more conventional stellarators. However, even in such an optimized stellarator, there will remain some non-zero departure from perfect symmetry. These deviations will lead to somewhat enhanced levels of beam ion losses above those present in an equivalent symmetric tokamak. For example, localized magnetic wells in the stellarator can result in small fractions of locally trapped orbits that drift directly out of the plasma; this ripple can additionally cause banana orbits trapped in the 1/R wells to gradually leave the plasma due to the successive perturbations in their bounce points. Barely passing particle orbits are also perturbed by low levels of this ripple; their orbits can become stochastic over many toroidal transits and leave the plasma.

The above orbital effects require careful analysis for neutral beam heating since they are especially exacerbated by the nearly collisionless nature and high transit speed of the beam ions. This forms the motivation for the following set of calculations. The model described below will be used for estimations of beam heating efficiencies (important for plasma performance estimations), scaling of heating efficiency with machine size and magnetic field level, parameter studies of the optimum beam injection tangency radius and toroidal injection location, and loss patterns of beam ions on the vacuum chamber wall (important for placement of wall armor and for minimizing the generation of impurities by the energetic beam ions).

I. Description of Model

Our model is based on the geometry shown in Figure 1. A pencil beam (zero width) is injected into the plasma on the equatorial plane ($\theta = 0$) aimed at a particular toroidal angle $\zeta_{inj.}$ and tangency radius, R_{tan} which can be varied. The deposition profile for the beam is an externally specified profile that we have obtained from the modeling of similar axisymmetric systems with TRANSP[2]. Particles are initially distributed over flux surface locations in consistency with this deposition profile. Only flux surfaces having major radii (at $\theta = 0$) $> R_{tan}$ are populated with beam ions. The initial beam ion pitch angle distribution in $v_{\|}/v$ is then determined by taking the ratio of the beam tangency radius to the local value of major radius where the particle is born.

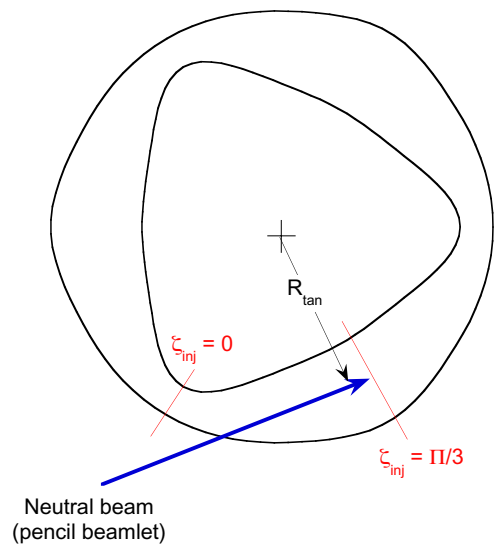

Figure 1 – Geometry used for NCSX neutral beam calculations.

From these initial conditions, the beam particle orbits are then followed by solving Hamiltonian guiding center equations which time advance the particles in the two angular coordinates (poloidal and toroidal angles in Boozer coordinates) and the the conjugate momenta. Equilibrium magnetic fields are obtained from the VMEC stellarator equilibrium code[3] which are then transformed to Boozer coordinates.[1] Collisions with a static background plasma consisting of electrons and two background ion species (a main ion and one impurity component) are simulated using a Monte Carlo collision operator[4] based on pitch angle and energy scattering terms, taking into account the full velocity-dependent potentials[5] without assumptions regarding relative orderings of the electron, beam ion and impurity velocities. Collisions are allocated on a fixed time step Δt_{coll} which is chosen so as to maintain $\nu\Delta t_{coll} << 1$ and to allow a smooth granularity in modeling the collisional processes. The time integration step for the orbit integration is controlled by the ordinary differential equation solver LSODE[6] which internally choses an integration time step so as to maintain a prescribed accuracy level. The typical variation of the different beam ion collision frequencies with velocity and flux surface included in this model are shown, respectively, in Figures 2(a) and 2(b).

The subscripts on the collision frequencies denote the species (electrons, ions, impurities) which the beam is colliding with and whether the collision frequency pertains to pitch angle deflection (D) or energy scattering (E). Currently we do not include collsions with neutrals. Typically, the

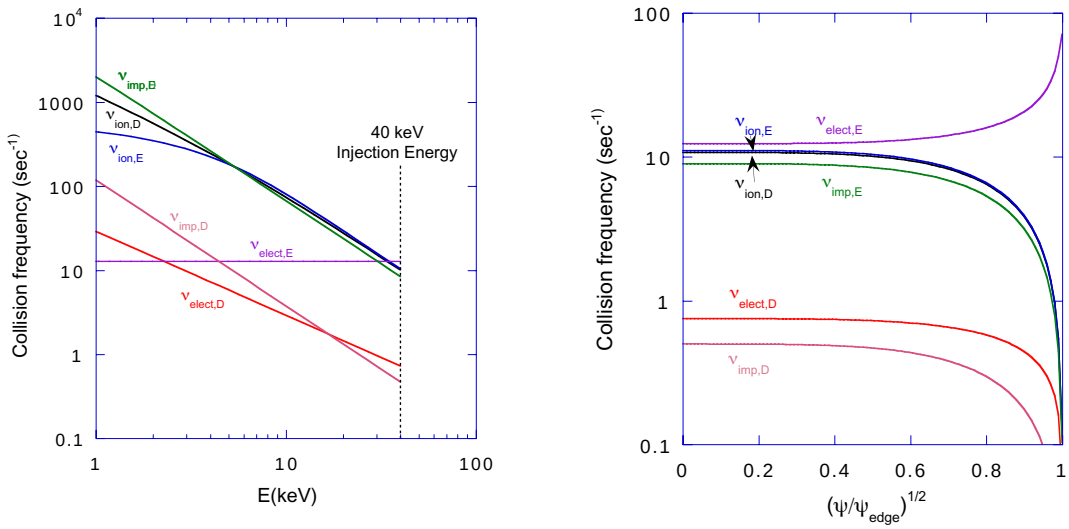

Figure 2(a) - Collision frequencies vs. energy at r/a = 0.5; 2(b) Collision frequencies vs. flux surface at E = 40 keV.

beam ions are injected at a velocity where they are slowing down somewhat more on electrons than ions, but they soon pass through the critical energy, below which they begin slowing down more on ions. Also as the beam ions pass through the critical energy, pitch angle scattering begins increasing; this can result in higher fast ion losses as the ions get scattered out of the passing region of velocity space. As the beam ions slow down to 3/2 kT_{ion} (with T_{ion} being the background field ion temperature), they are counted as part of the background plasma species. Beam ions that pass through the outer flux surface are removed from the distribution and not replaced. Beam heating efficiencies are calculated by recording the losses of particles and energy out of the outer magnetic flux surface that occur during the slowing-down process. The DELTA5D[7] code follows groups of beam particles on different processors in parallel using the MPI language for inter-processor communication. It has been adapted to both the Cray T3E and IBM-SP computers. A variety of diagnostics of the escaping particles, such as pitch angle, energy and particle lifetime distributions, are retained to aid in understanding the loss mechanisms.

In Figures 3(a) and 3(b) we show some of the characteristics of a slowing-down beam for the parameters $n(0) = 6 \times 10^{19}$ m^{-3}, $T_e(0) = T_I(0) = 2.4$ keV. Figure 3(a) shows on the left hand scale the time evolution of the percentage of energy lost from the beam averaged over the ensemble of 4,096 particles used here. We normally follow the distribution of beam particles until this energy loss fraction reaches a saturated plateau; this flattening is associated with the average beam ion slowing down to the 3/2 kT_{ion} energy level [shown on the right-hand scale in Figure 3(b)]. Figure 3(a) also shows the time variation of the ensemble averaged ratio of magnetic moment to energy for the beam. Initially this ratio starts out small due to the anisotropic nature of the beam (i.e., composed mostly of passing orbits) and then increases as the beam pitch angle scatters and spreads out to become more isotropic. Finally, Figure 3(b) shows the decrease in time of the number of beam particles, indicating the degree to which particles are lost at times prior to that required for slowing down enough to join the background distribution.

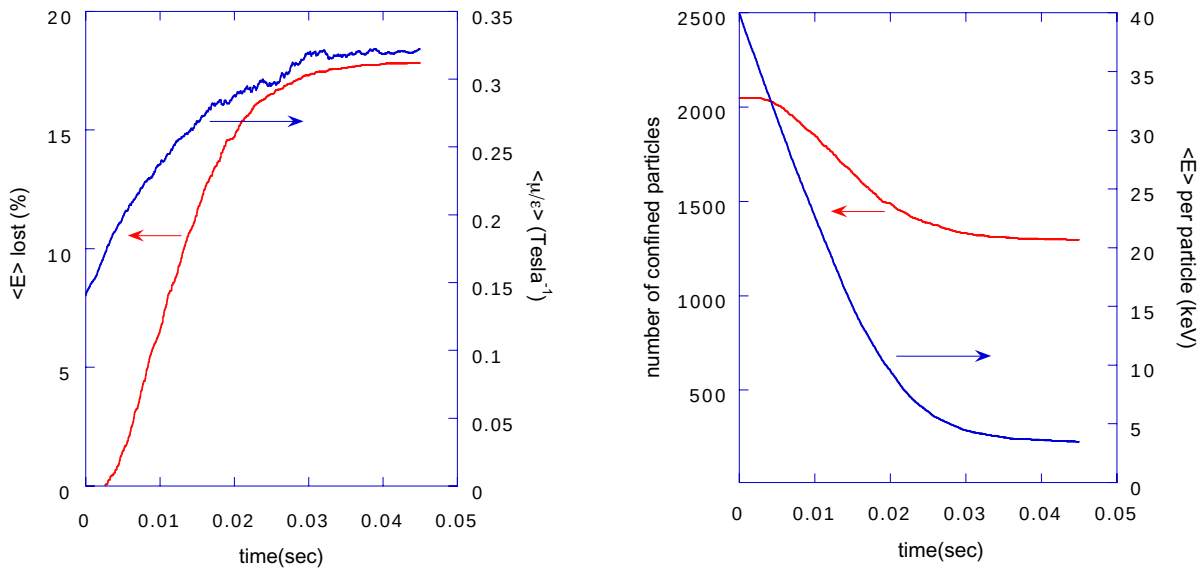

Figure 3(a) - Typical evolution of ensemble averaged beam energy loss and <μ/ε>; 3(b) - Decay in time of the number of confined beam particles and average energy per particle.

Figures 4(a) and 4(b) show histograms of the energy and pitch angle distributions of the escaping beam ions for the case shown in Figure 3.

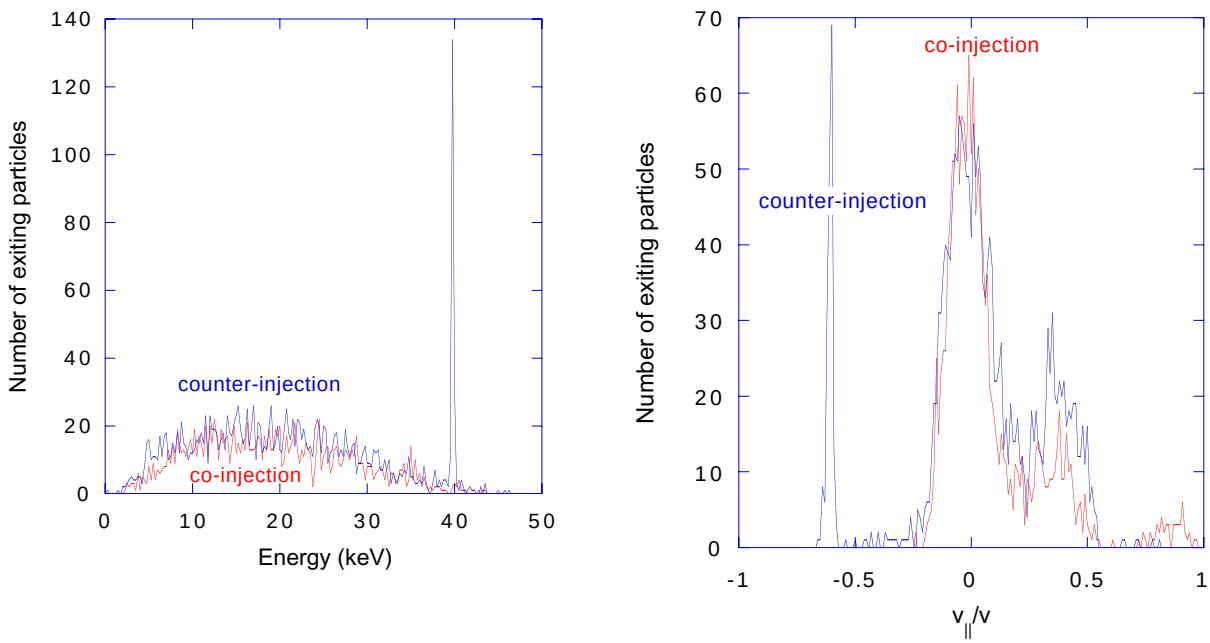

Figure 4(a) - Energy spectrum of exiting beam particles; 4(b) - Pitch angle spectrum of exiting beam particles.

As can be seen, the energy losses are characterized by a broad peak centered around 15 - 20 keV for both co- and counter- injection. The counter-injected ions also show a very sharp peak at the injection energy, presumably associated with prompt losses. The pitch angle distributions of escaping ions shown in Figure 4(b) are mostly peaked around the deeply trapped range of pitch

angles with a secondary peak (for the co-injected ions) more in the transitional region. The counter-injected ions show a very sharp peak near $v_{\|}/v = 0.6 - 0.7$ which is close to the birth pitch angle, indicating a prompt loss component for the case of a tangency radius $R_{tan} = 1.7$ m.

II. Parameter Scans

We have used the model described above to study sensitivity to variations in configuration, beam and plasma parameters. Except where otherwise indicated, we have chosen to make our variations about an NCSX configuration known as LI383 with a volume averaged magnetic field of 2 Tesla, and an average major radius of 1.7 meters. The central plasma density is nominally 6×10^{19} m^{-3} and the central ion and electron temperatures are set to 2.4 keV; the plasma species is hydrogen. An impurity species is present with Z = 18, A = 9, at 1% of the electron density, and a temperature equal to the background ion temperature. The beam is also taken as hydrogen and is monoenergetic at injection with an energy of 40 keV. The beam is initially deposited at $\theta_{inj} = 0$, $\zeta_{inj} = \Pi/3$. Plasma profiles for temperature and density go as $1 - \psi^2$ and the ambipolar potential is set to zero.

In Fig. 5(a) the variation of beam losses with machine size is shown for both co- and counter-injected beams. Here we have plotted results both at constant plasma density and with density varying inversely with machine size so that the ratio of the collisional path length to the machine size remains constant.

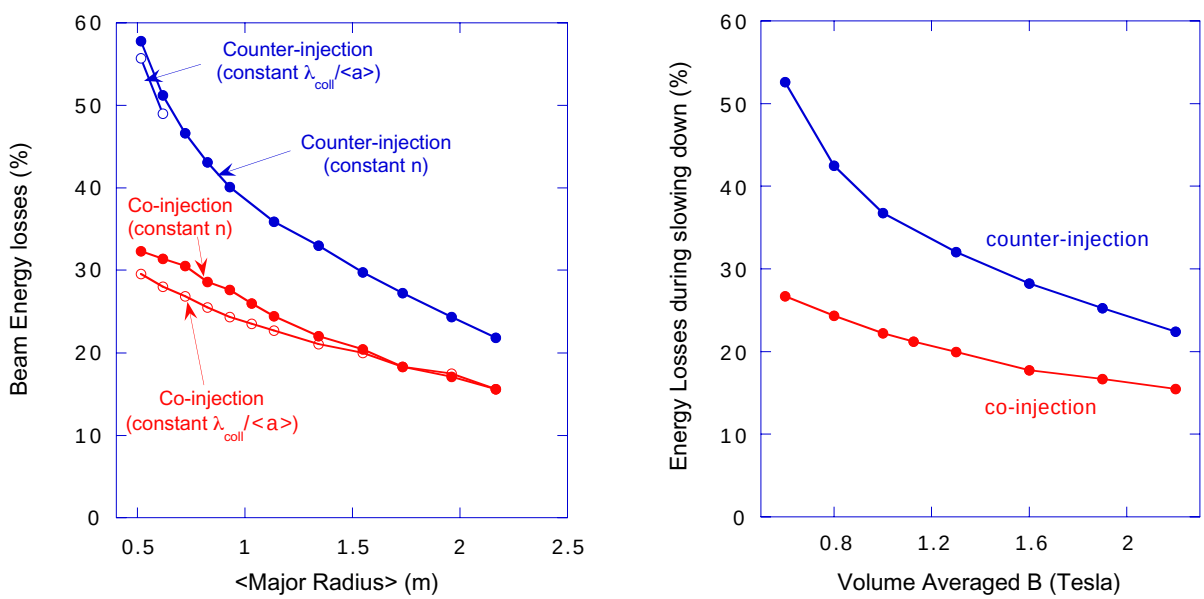

Figure 5(a) - Beam energy loss scaling with machine size for a 40 keV hydrogen beam; 5(b) - Beam energy loss scaling with volume averaged magnetic field.

The latter constraint is chosen so as to maintain similar collisional orbit characteristics (i.e., constant ratios of collision frequency to bounce and transit times). As can be seen, losses are progressively higher for both co- and counter-injected beams as the machine dimensions are made smaller or, equivalently as the beam ρ^* parameter $\rho^*_{beam} = \rho/R_0$, ρ = beam gyroradius is increased. In Fig. 5(b) the machine size is fixed (major radius = 1.73 m) and a scan is made in

the magnetic field strength. Again, there is an inverse scaling with ρ^*_{beam} for both co- and counter-injected ions. For both Figs. 5(a) and (b) the initial beam energy is 40 keV. In these plots we have covered roughly the same range of ρ^*_{beam} values.

In Figure 6(a) the sensitivity of losses to the beam tangency radius for co- and counter-injected beams in a <B> = 2T and R_0 = 1.73 m device is examined. As the tangency radius is made smaller, the beams are initially launched onto larger pitch angles relative to the magnetic field (smaller $v_{\|}/v$). This puts them closer to the trapped-passing transitional regime of velocity space where orbits are more likely to experience prompt losses. As may be seen, the losses steadily increase for both co- and counter injected ions as R_{tan} is decreased. The minimum of these curves is close to the point where R_{tan} = the magnetic axis location. For this configuration the magnetic axis at the toroidal injection angle ($\zeta_{inj} = \Pi/3$) was 1.68 m. As R_{tan} is increased beyond this point, losses again increase due to the fact that the beam ions are progressively being aimed further out in minor radius leading to hollow deposition profiles and increased fractions of prompt orbit losses.

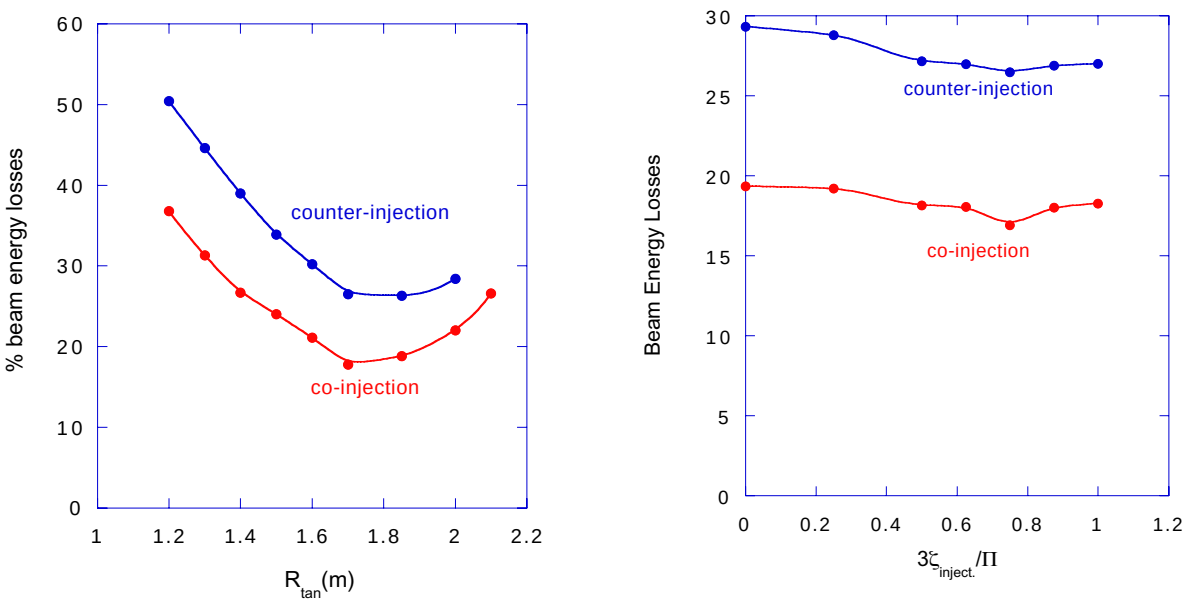

Figure 6(a) - Dependence of beam losses on beam tangency radius; 6(b) - Dependence of beam losses on toroidal injection location.

In Figure 6(b) we vary the toroidal angle at which the beam ions are initially deposited, going from the beginning of the field period (ζ_{inj} = 0 symmetry plane) to the half field period point ($\zeta_{inj} = \Pi/3$); these two angles have been shown in Figure 1. Beam losses only depend weakly on the injection location due to the fact that most losses only occur after many transits around the stellarator after which collisions presumably will have spread out the beam distribution more uniformly in toroidal angle and erasing any memory of the initial particle loading. Nevertheless, there is some variation of losses with changes in ζ_{inj} and it appears that there is an optimum around $\zeta_{inj} = \Pi/4$ for both co- and counter-injected beams. The reasons for this slight minimum in losses have not been investigated yet, but are expected to be caused by the dependencies of the first orbit losses on the injection angle.

In Figure 7 we investigate the variation of beam losses with injection energy. Results presented in the previous Figures have been based on a 40 keV injection energy. The beams anticipated for NCSX will be capable of going up to 50 keV, but will also include lower energy components. For these calculations, we have also shifted our plasma and machine parameters to a device with R_0 = 1.4 meters, <B> = 1.23 Tesla, average temperature for ions and electrons = 1.26 keV and average electron density = 6.8 x 10^{19} m^{-3}; these correspond to peak temperatures and densities of 1.58 keV and 8.5 x 10^{19} m^{-3} respectively. Although the device size and magnetic field strength are smaller for this case, the beam losses are also lower due mostly to the fact that the slowing down time is shorter for these parameters. Another factor which keeps beam losses lower here is that the critical energy (E_{crit}) where the fast ions begin slowing down more on background ions than electrons is lower. For these parameters, it is around 23 keV while for the earlier parameters [n(0) = 6 x 10^{19} m^{-3}, $T_e(0) = T_I(0)$ = 2.4 keV] E_{crit} was around 34 keV. This lower E_{crit} also is likely to account for the fact that beam losses seem to actually get slightly lower with increasing energy for the co-injected beams from 30 up to 50 keV. This is caused by the fact that below E_{crit} pitch angle scattering rapidly increases resulting in beam ions being scattered into the more lossy transitional and trapped orbits. As the initial beam energy is increased above E_{crit}, the beam ions can undergo more energy slowing down without as much pitch angle scattering, resulting in a smaller proportion of the initial beam energy being lost through scattering into unconfined orbits.

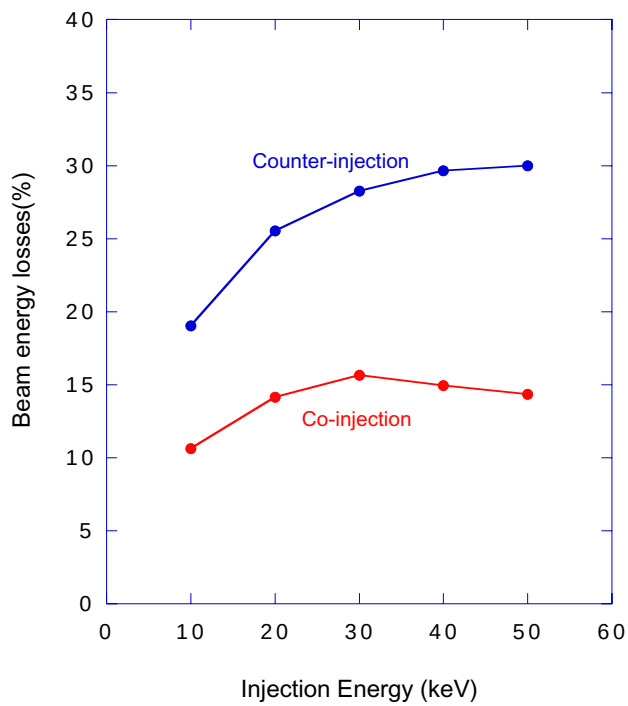

Figure 7 - Variation of beam energy losses with injection energy for a recent machine design point at R_0 = 1.4 m, <B> = 1.23 T, n(0) = 8.5 x 10^{19} m^{-3}, $T_e(0) = T_I(0)$ = 1.58 keV.

III. Loss Patterns of Beam Ions on Outer Flux Surface

As indicated in Figure 4(a), a large fraction of the escaping beam ions leave the plasma with 1/3 to 1/2 of their initial injection energy. It is desirable to intercept this power deposition on the vacuum chamber wall by localized protective armor plating to minimize impurity generation and wall erosion. In order to design such structures, it is necessary to make estimates of the wall locations where the escaping beam ions will be deposited. Within the above Monte Carlo model, as the beam ions leave the outermost closed flux surface, their exit locations, exit times, pitch angles and energies are recorded. If it is assumed that beam ions then move rapidly through the unclosed outer flux region, this information can be useful in estimating power loading patterns on the vacuum chamber walls. More realistic models may eventually be developed which follow the fast ion trajectories in the outer region where flux surfaces no longer exist. Results based upon the current model are shown in Figure 8 for a typical case. Here the exit locations are plotted in Boozer poloidal and toroidal angle coordinates for the outermost flux surface. Colors are used to indicate the energy at which the fast ions leave the surface. As can be seen, most of the ions leave at intermediate energies from 10 – 20 keV, in similarity with Figure 4(a).

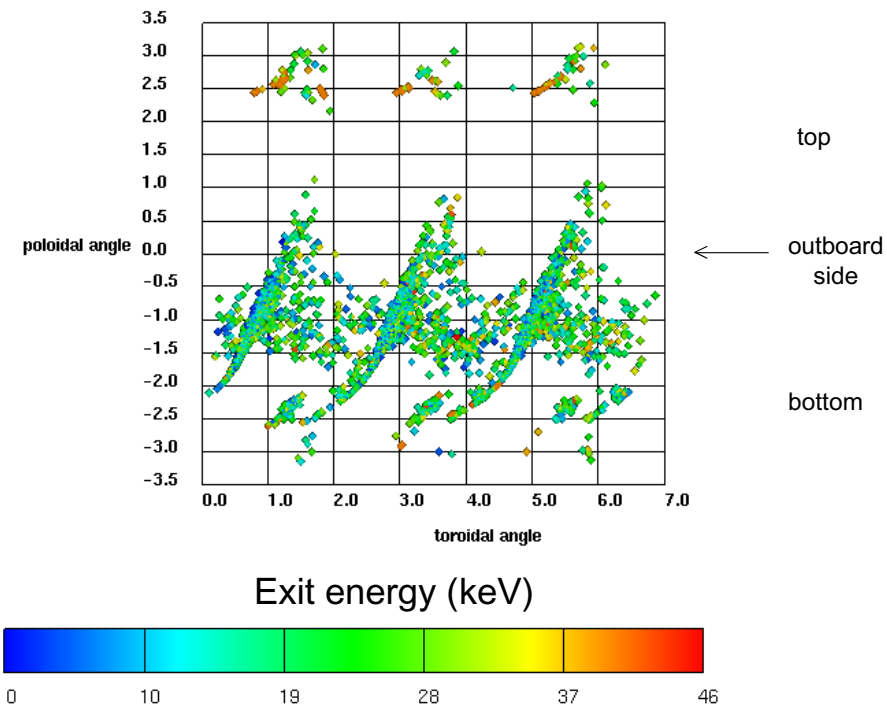

Figure 8 - Location and energy spectrum of beam losses on outer surface in 2D Boozer coordinates

The fast ion losses are primarily concentrated in helical stripes on the bottom of the stellarator with one stripe per field period (this would presumably shift to the top of the stellarator with reversal of the magnetic field direction). We have also transformed this data into more geometric coordinates. In Figure 9 we plot the data of Figure 8 vs. the normal cylindrical azimuthal coordinate, $\phi_{cylindrical}$ and a poloidal angle, θ, which is equal to $\tan^{-1}[z/(R-R_0)]$.

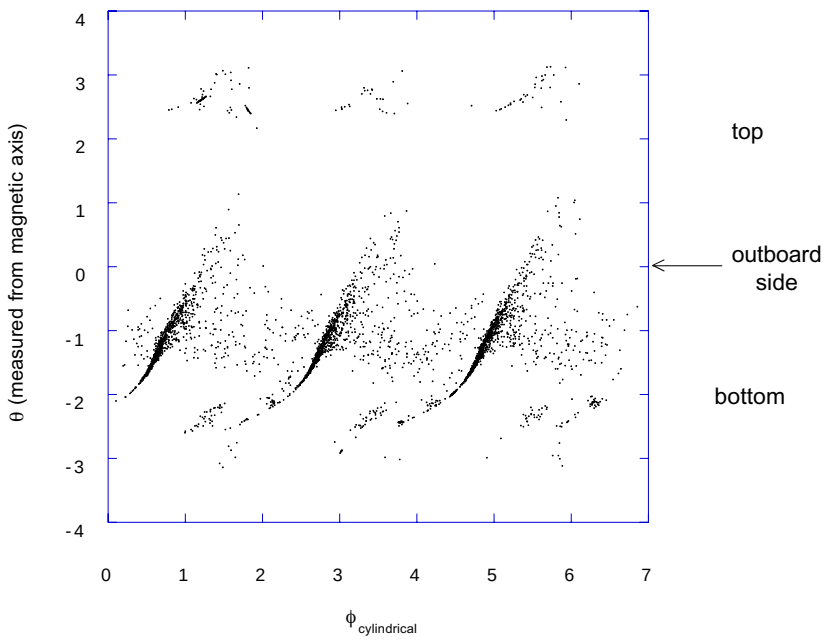

Figure 9 - Location of beam losses on outer surface in 2D real space coordinates.

Finally, we have plotted the ion loss locations on the three-dimensional outermost flux surface (Figure 10) as obtained from the VMEC stellarator equilibrium code. The flux surface is shown in red and the ion exit locations are color coded according to the ion's energy at the time it passes through the flux surface. Again, it can be seen that the losses are somewhat concentrated, motivating the design of protective structures at these locations.

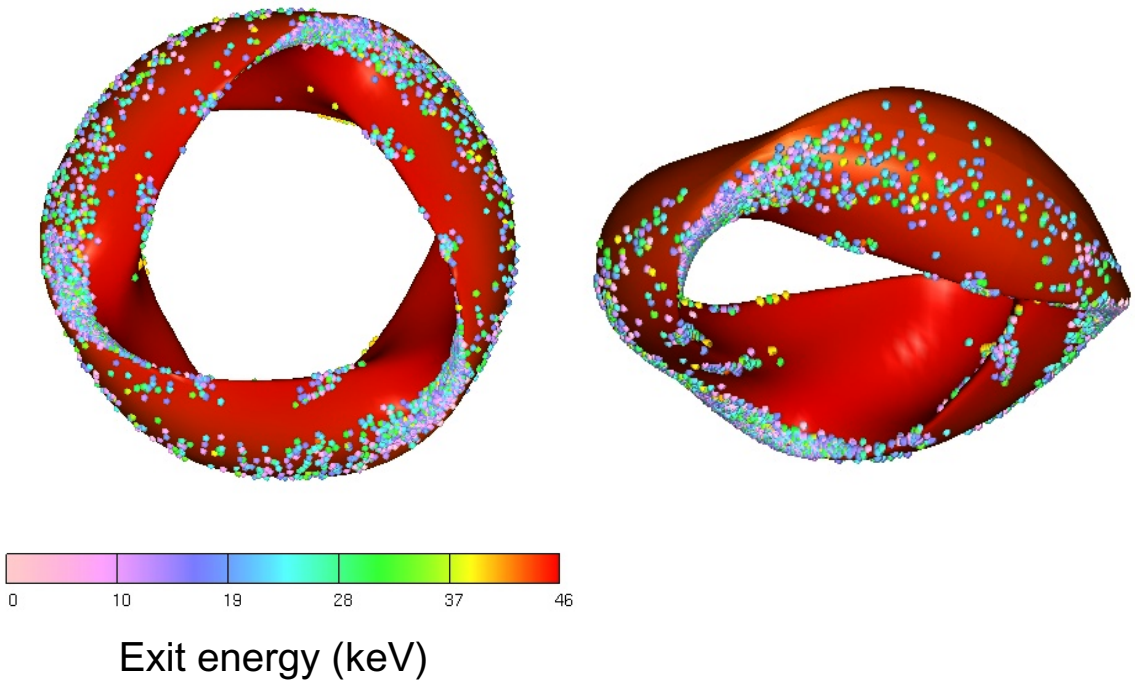

Figure 10 - Location and energy spectrum of beam losses on outer surface in 3D

IV. Suggestions for Future Work

The model described here has been developed for comparative studies of different NCSX configurations and to obtain approximate estimates of beam heating efficiencies and loss patterns. In order to develop an adequate physics understanding of fast ion confinement in a real experiment, a number of upgrades and new tools will need to be developed. Although many of these issues have already been thoroughly examined for tokamaks, the inherently 3D nature of the stellarator geometry will, in many cases, require a complete re-development of existing tools.

In the area of neutral beam deposition, finite width, multiple energy group beam models will need to be developed and their intersection with the 3D flux surface shapes taken into account. As the beam ions slow down, collisions with neutrals and multiple impurity species should be modeled; beam-beam self collsions and finite beam gyroradius effects may also be of relevance for some regimes. A number of additional physics diagnostics for beam ion effects can readily be included in the Monte Carlo calculations. For example, beam-driven currents and transfer rates of beam energy to the different plasma species can be obtained. Other diagnostics, such as predictions of the energy distributions of charge exchange neutrals escaping the plasma, can be useful in interpreting charge exchange measurements.

The beam slowing down model described here assumes nested, closed flux surfaces. Stellarators are expected to develop magnetic islands and open field lines at some point near the plasma egde. In determining beam loss rates through these regions as well as beam loss patterns and heat loads on walls and divertors, it will be important to follow beam ion orbits into these regions by matching together Hamiltonian orbit models for the inner closed surface region with more conventional real space guiding center drift models for the regions outside the last closed flux surface.

Fast ion losses will also be influenced by instabilities and turbulence in the plasma. Some of the larger scale instabilities which may be present in certain regimes of NCSX operation are tearing and kink instabiltities. Also, fast ions in stellarators are known to excite various Alfvén instabilities through wave-particle resonances. Due to the fact that the equations describing the Alfvén eigenmode structure depend on metric elements in addition to $|B|$, it should be expected that different types of Aflvén modes will be possible in NCSX than in a tokamak, even though $|B|$ itself may have a similar symmetry as the tokamak. These instabilities will require analysis tools which take into account the strong 3D shaping effects of low aspect ratio stellarators. The large harmonic content characteristic of low aspect ratio devices might be expected to widen lower order Alfvén gaps and open up higher frequency gaps caused by noncircular shaping. Also, high radial resolution is necessary to resolve the complex continuum/gap structures which result from the fact that all toroidal modes must be taken into account simultaneously (i.e., unlike the tokamak, the toroidal mode number is no longer a good quantum number). A code is under development to calculate the continuum gap structure for low aspect ratio stellarator hybrids using VMEC data and coordinates. Once this structure is understood, the next steps are to calculate the eigenmodes and examine their stability properties with particle-wave excitation.

Mode structures for these instabilities can then be included in the Monte Carlo calculations and their influence on fast ion confinement examined.

---

[1] A. H. Boozer, Phys. Fluids **24**, 1999 (1981).
[2] R. V. Budny, D. C. McCune, M. H. Redi, J. Schivell, R. M. Wieland, Phys. Plasmas, **3**, 4583 (1996).
[3] S. P. Hirshman, J. C. Whitson, Phys. Fluids **26**, 3553 (1983).
[4] A. H. Boozer, G. Kuo-Petravic, Phys. Fluids **24**, 851 (1981).
[5] S. P. Hirshman, D. J. Sigmar, Phys. Fluids, **19**, 1532 (1976).
[6] A. C. Hindmarsh, "Odepack, a Systematized Collection of ODE Solvers, in Scientific Computing," R. S. Stepleman et al. (Eds.), North-Holland, Amsterdam, 1983, pp. 55-64.
[7] D. A. Spong, J. Carlsson, D. B. Batchelor, et al., Bull. Am. Phys. Soc. **44**, 215 (1999).